Int J Adv Manuf Technol (2015) 81:825–831
DOI 10.1007/s00170-015-7286-9

ORIGINAL ARTICLE

Microstructure and mechanical properties of laser-MAG hybrid welded thick-section weathered steel joint

X. Y. Gu[1] · Z. Z. Duan[2] · X. P. Gu[1] · X. H. Zhang[3] · Y. L. Xie[3] · D. Q. Sun[1]

Received: 10 June 2013 / Accepted: 5 May 2015 / Published online: 14 May 2015

Abstract Weathered steel (S355J2W) joint was prepared by laser-metal active gas hybrid welding technique. The microstructures of the joint were examined with an optical microscope and a scanning electron microscope. Microhardness measurement, tensile test, side bend test, and Charpy impact test were conducted to examine the mechanical properties of the joint. Experimental results show that S355J2W steel joint has a nail head shape with three different zones: weld metal, heat-affected zone (composed of overheated zone, normalized zone, and incomplete normalized zone), and base metal. The highest microhardness of the joint is 280 HV. All the joint specimens failed in the base metal. Average tensile strength of 502.6 MPa and yield strength of 380.9 MPa were achieved. A bending angle of 180° was obtained for all the joint specimens, and a crack less than 3 mm was detected. The average values of absorbed energy for the weld are 198.7 and 79.1 J at −40 and −20 °C, respectively. All the specimens exhibited a level of toughness as indicated by deformation at the fracture surface.

✉ X. P. Gu
gxp@163.com

[1] Key Laboratory of Automobile Materials, School of Materials Science and Engineering, Jilin University, Changchun 130022, China

[2] College of Mechanical and Electrical Engineering, Changchun Institute of Technology, Changchun 130012, China

[3] Changchun Railway Vehicles Co., Ltd., Changchun 130062, China

Keywords Microstructure · Mechanical property · Laser-MAG hybrid welding · Weathered steel

1 Introduction

Weathered steel, as a low-carbon and low-alloy steel, has high strength and corrosion properties. The addition of alloying elements Cu, P, Cr, Ni, and so on promotes the formation of a stable and protective oxide layer after exposure in the atmosphere; the formed oxide layer can remarkably reduce corrosion rate [1, 2]. S355J2W steel is weathered steel created according to European standard EN10025 and is widely utilized in structures such as railway vehicles, bridges, and buildings.

Laser hybrid arc welding combines an electric arc with a laser beam. Deep weld penetration, minimal deformation, high welding speed, the ability to bridge relatively large gaps, capability to weld highly reflective materials, and improvement of arc stability can be acquired when two techniques are combined [3, 4].

Several experiments have been conducted to study the joint quality of laser hybrid arc welding for aluminum alloy, magnesium alloy, and steel with thickness less than 10 mm [5–7]. Modeling and numerical studies have also been conducted on hybrid welding processes such as thermal distribution, heat-combining characteristic mechanism, and residual stress in the weld joint [8–10].

Laser hybrid arc welding of thick-section steel was performed in this study. The microstructure and mechanical properties of the joint were analyzed. The data obtained from this study can be utilized as a scientific basis to optimize the

Table 1 Chemical compositions of S355J2W hot rolled plate (wt%)

C	Si	Mn	P	S	Cr	Cu
0.16	0.50	0.50–1.50	≤0.03	0.03	0.40–0.80	0.25–0.55

welding process and promote the application of laser hybrid arc welding.

2 Experimental procedure

The chemical compositions of S355J2W hot rolled steel plate utilized in this investigation are listed in Table 1. NiCu1-IG wire was employed as metal filler. The base metal was cut into 16-mm-thick 300 mm × 100 mm rectangular specimens. One-side welding with three passes was conducted using laser-metal active gas (laser-MAG) hybrid welding technique with gas mixture of Ar/CO_2 (85/15). The parameters of the welding process are listed in Table 2.

The microstructures of the joint were examined with an optical microscope and a scanning electron microscope (SEM). Microhardness was measured according to the EN 10043-1 standard. Tensile tests with three specimens were conducted in an HY-1000 universal test machine according to the EN895-1995 standard. The sheet specimens were 25 mm wide with 80-mm gauge length. Side bend tests with three specimens were conducted according to the EN910-1996 standard. Charpy-V specimens were tested in an impact machine at −20 and −40 °C according to the EN 875-1995 standard. The notch was located at the weld centerline (notch in weld).

3 Results and discussions

3.1 Joint microstructure

Figure 1a presents a micrograph of the laser-MAG hybrid welded S355J2W steel joint. The cross section of the joint has a nail head shape and contains three different zones: weld metal (WM), heat-affected zone (HAZ), and base metal (BM). XRD analysis revealed a structure of α-Fe in the joint as shown in Fig. 1b.

An optical photograph of the BM is shown in Fig. 2a. Ferrite–pearlite can be observed in the photograph. The white and gray polygonal grain with fine grain size is ferrite. The dark and banded structure embedded in the ferrite is pearlite. The SEM photograph in Fig. 2b shows lamellar pearlite.

The experimental results indicate that the microstructure of WM is columnar. The grain grows vertically with the fusion line because of heterogeneous nucleation (Fig. 3a). An equiaxed grain is formed along the weld centerline at the bottom of the joint (Fig. 3b). It is noted that the appearance of upper part of the weld is similar to that of MAG welded joint and the appearance of lower part of the weld is similar to that of laser welded joint. Lower laser power and larger arc current in the upper part of the weld resulted in larger weld width. However, larger laser power and lower arc current in the lower part of the weld resulted in larger penetration. This causes the difference in the weld of laser MAG hybrid-welded joint compared to laser welded joint as reported by several investigators [11]. The microstructure of the cover layer formed in the third pass mainly contains pearlites and various ferrites such as primary ferrite (PF) in the grain boundary of the original austenite, acicular ferrite (AF) in grains, and several com-shaped ferrite side plates (FSPs). A PF with a long strip or polygonal shape is produced in the grain boundary because of the high energy of the said boundary. AF with grain width of 2 μm is obtained in the grain of the original austenite. Considering that nucleation of AF can occur anywhere, its growth was restricted by each other to form a fine-grained AF. FSP with a large aspect ratio propagates from the grain boundary to the grain (Fig. 3c, d). FSP is a ferrite formed by propagation from the grain boundary to the grain and is basically a Widmanstatten structure [12].

Given that multi-pass welding technology was utilized in this experiment, remelting or reheating of the former pass during the next pass could occur. The microstructure of the

Table 2 Parameters for laser-MAG hybrid welding

Pass	Laser power (W)	MAG welding current (A)	MAG welding voltage (V)	Welding speed (m min^{-1})	Defocusing distance (mm)	Laser focus position (mm)	Distance from laser beam spot to MAG arc (mm)	Angle between the electrode and the welding direction (°)	Argon shield flow (L min^{-1})
1	6.0	240	21	1.2	−2	250	2	60	15–20
2	2.0	270	24	0.4	−2	250	2	60	15–20
3	2.0	270	24	0.4	−2	250	2	60	15–20

remelting and reheating zone would then change. Figure 3e, f presents a photograph of weld metal formed during the second pass (the second-pass region) adjacent to that formed during the third pass. When peak temperature is between melting temperature and 1100 °C during third pass welding, the transformation of α (ferrite) → γ (austenite) occurs. Grain coarsening of austenite also occurs in the second-pass region. Coarse striped and AF and some bainites are formed during subsequent cooling. When peak temperature ranges from 1100 to A3 (critical temperature of transformation between ferrite and austenite), the growth of austenite does not happen during the heating process. Therefore, ferrites and pearlites with fine grain size are obtained during cooling. This process is similar to the normalization process.

HAZ of the joint is composed of the overheated zone, normalized zone, and incomplete normalized zone. The overheated zone is heated to peak temperature ranging from 1100 °C to melting temperature during welding. Its microstructure is shown in Fig. 4. The microstructure of the overheated zone is basically a Widmanstatten structure with some pearlites and bainites. Austenite in the overheated zone grows rapidly during heating. Coarse austenite transforms into a Widmanstatten structure during subsequent cooling. During the formation of a Widmanstatten structure, ferrite grows along the {111} crystal face of austenite by shear mechanism and will eventually grow from the grain boundary. Parallel flake ferrite is formed within an austenite grain. Residual austenite in the ferrite transforms into pearlite. Carbide or oxide dissolves into austenite because of the high temperature, which increases the carbon content of the austenite to change the austenite's continuous transformation curve. Thus, some bainites are formed during rapid cooling.

The normalized zone acquires a peak temperature ranging from A3 to 1100 °C. The growth of austenite ceases during heating. Therefore, ferrites and pearlites with fine grain size are during cooling (Fig. 4c).

An optical photograph of the incomplete normalized zone with retained ferrite and transformed ferrite and pearlite is shown in Fig. 4d. The microstructure is mixed with various ferrites with large (retained ferrite) and small (transformed ferrite and pearlite) grain sizes. Considering that retained ferrite exists, a banded structure is observed although partial recrystallization occurred.

3.2 Mechanical properties

Figure 5 presents the obtained results in the microhardness measurement of the joint. Microhardness was measured

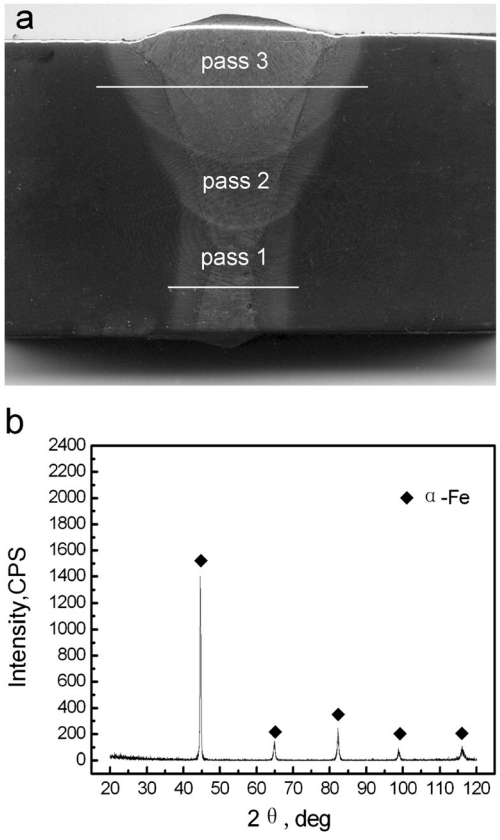

Fig. 1 Laser-MAG hybrid welded S355J2W steel joint: **a** cross section photograph of the joint and **b** X-ray diffraction diagram obtained on the joint cross section

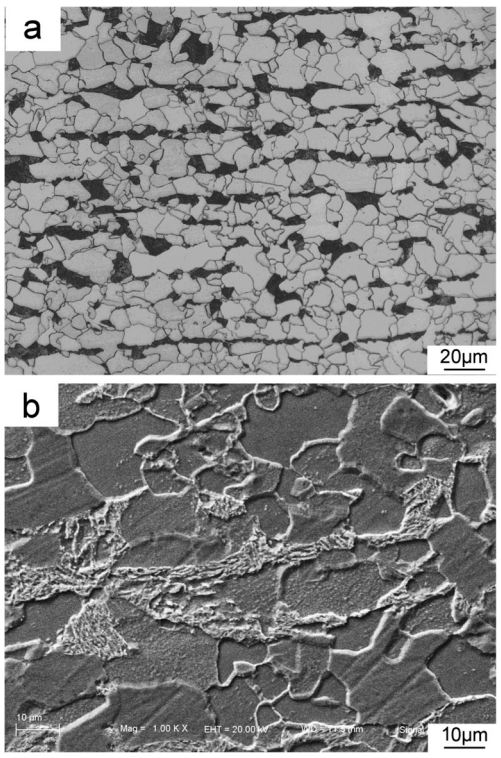

Fig. 2 Microstructure of the base metal: **a** optical photograph and **b** SEM photograph

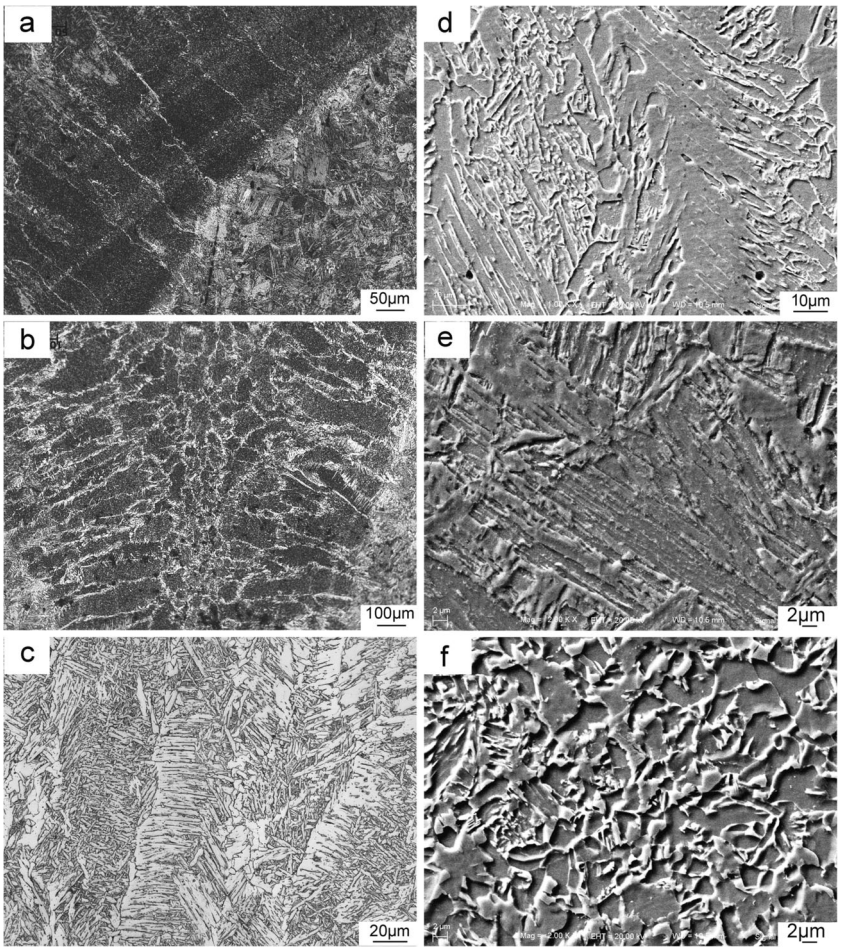

Fig. 3 Microstructure of the weld: **a** crystallization character of the upper part of the weld, **b** crystallization character of the lower part of the weld, **c** optical photograph of the cover layer, **d** SEM photograph of the cover layer, **e** SEM photograph of the remelting zone to form coarse grain, and **f** SEM photograph of the remelting zone to form fine grain

according to the EN 10043-1 standard along a line at the joint cross section 2 mm from the upper surface and 2 mm from the lower surface as shown in Fig. 1a, respectively. Microhardness in the overheated zone is the highest, a result

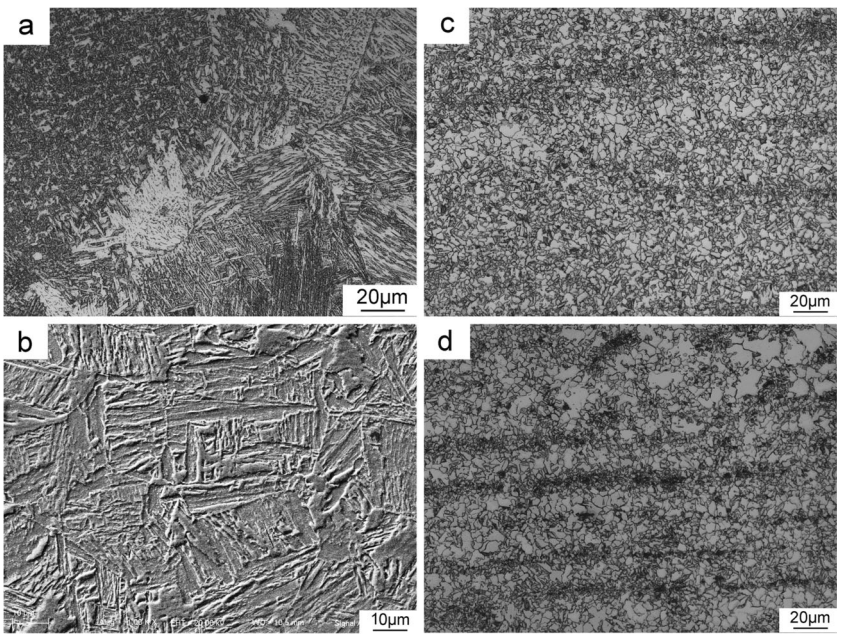

Fig. 4 Microstructure of HAZ: **a** optical photograph of overheated zone, **b** SEM photograph of overheated zone, **c** optical photograph of the fine grain zone, and **d** optical photograph of the incompletely normalized zone

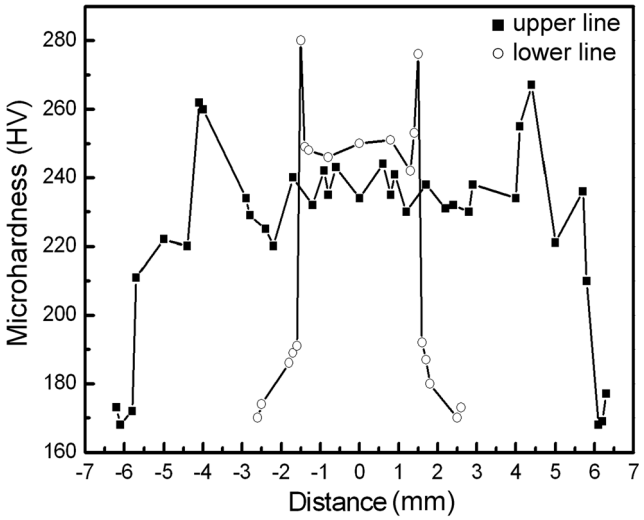

Fig. 5 Microhardness of the joint

that can be attributed to the Widmanstatten structure formed in the said zone. The microhardness of the fine-grained zone is lower than that of the overheated zone but higher than that of the incomplete normalized zone because of fine-grained equiaxed ferrite in the fine-grained zone. The microhardness of the overheated zone at the lower line is higher than that at the upper line. This finding can be ascribed to microstructure refinement with increased cooling speed. The highest microhardness of the joint is 280 HV, which meets the requirement of less than 380 HV according to the EN15614 standard.

Transverse tensile tests were conducted, and the results are presented in Table 3. The photograph of the specimens from the tensile tests is shown in Fig. 6. The joints do not neck in the weld or HAZ but do in the BM. All the specimens fail in the BM. This indicates that plasticity and strength in the joint are not even. The tensile strength of the weld and HAZ is larger than that of the BM. The plasticity of the weld and HAZ is lower than that of the BM. In other words, the failure in the BM is due to the strength overmatching of the weld zone [11, 13]. Tensile strength of 502.6 MPa and yield strength of 380.9 MPa represent the strength of the as-welded BM. The specimens exhibit obvious deformation at the fracture surface.

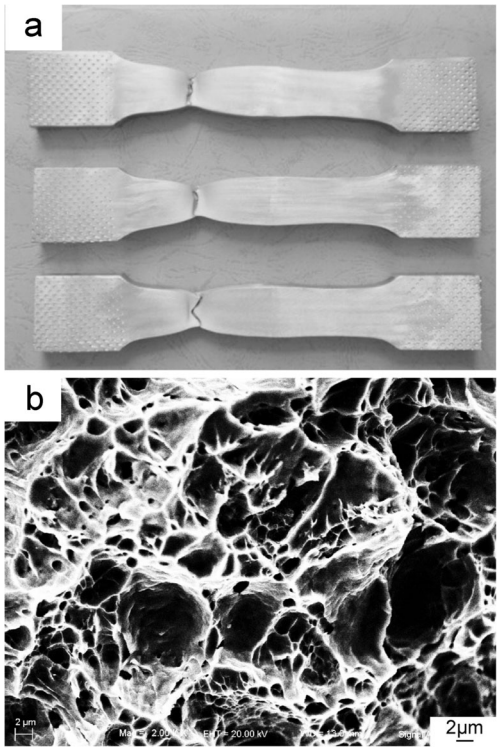

Fig. 6 Photograph of specimens from tensile tests: **a** fracture site of joints and **b** SEM photograph of joint fracture surface

Figure 7 shows the side bend-tested specimens. A bending angle of 180° is obtained for all the specimens. A crack with length of 2 mm appears in specimen 2, which meets the requirement of less than 3 mm according to the EN15614 standard. The crack appears in the region between the two weld layers. This result can be attributed to the stress in the said region.

Charpy-V tests that measure impact resistance were performed at −20 and −40 °C. The notch is located at the weld centerline. The average values of absorbed energy are shown in Table 4. Absorbed energy decreases from 198.7 to 79.1 J when test temperature decreases from −20 to −40 °C. Figure 8 shows the fracture surfaces of the specimens. All the specimens exhibit a level of toughness as indicated by deformation at the fracture surface.

Table 3 Tensile test data

	Ultimate tensile strength (MPa)		Yield strength (MPa)		Elongation (%)		Failure zone
	Single value	Average value	Single value		Single value	Average value	
Specimen 1	500.5	502.6	380.4	380.9	30.0	28.8	Base metal
Specimen 2	498.1		379.0		28.8		Base metal
Specimen 3	509.1		383.2		27.5		Base metal

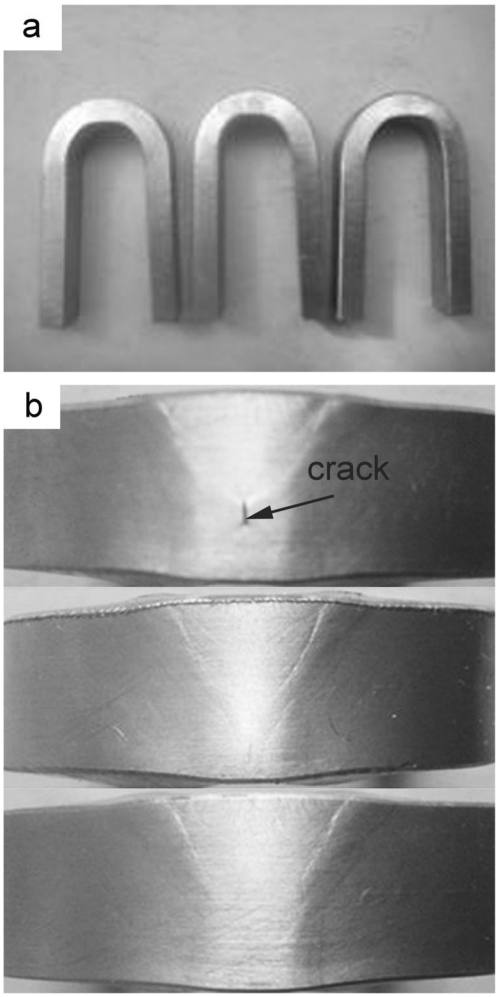

Fig. 7 Photograph of specimens from side bend tests: **a** a bending angle of 180° is obtained and **b** a crack of 2-mm length is observed

4 Conclusions

Thick-section weathered steel (S355J2W) was welded by laser-MAG hybrid welding. The following conclusions are drawn.

1. S355J2W steel joint has a nail head shape with three different zones: weld metal, HAZ (composed of overheated zone, normalized zone, and incomplete normalized zone), and BM.
2. The microstructure of the weld metal zone contains some pearlites and various ferrites, such as PF, AF, and some com-shaped FSPs. The microstructure of the overheated zone is basically a Widmanstatten structure with some pearlites and bainites. The microstructure of the normalized zone is composed of fine ferrite and pearlite, and the microstructure of the incomplete normalized zone is composed of retained ferrite and transformed ferrite and pearlite.
3. The highest microhardness of the joint is 280 HV, which meets the requirement of less than 380 HV.

Table 4 Impact test data

Test temperature (°C)		Energy absorbed (J)	Average value of energy absorbed (J)
−20	Specimen 1	174.7	198.7
	Specimen 2	174.0	
	Specimen 3	248.1	
−40	Specimen 4	70.8	79.1
	Specimen 5	79.9	
	Specimen 6	86.6	

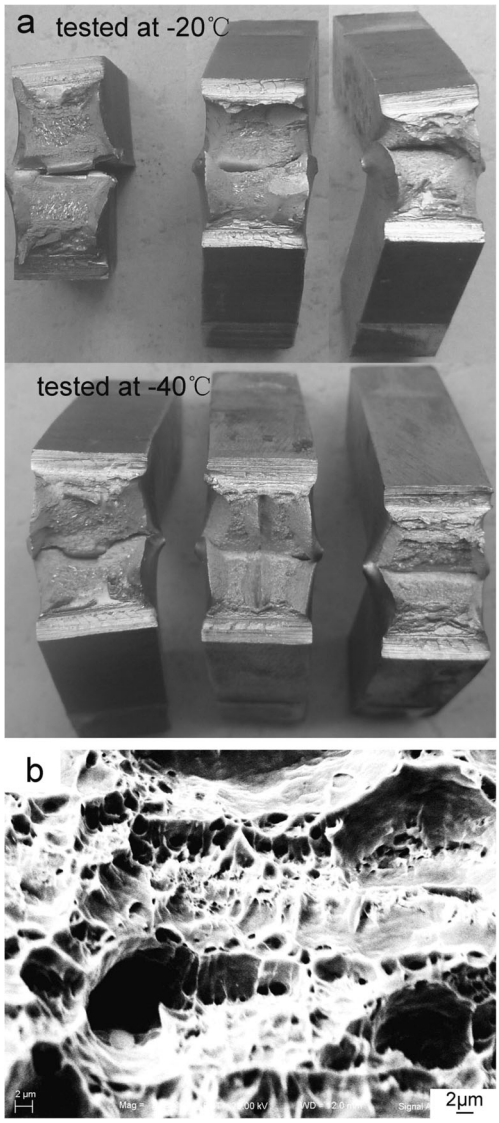

Fig. 8 Photograph of specimens from Charpy impact test: **a** microphotograph of joint fracture surface and **b** SEM photograph of joint fracture surface

4. All the joint specimens fail in the BM. Average tensile strength of 502.6 MPa and yield strength of 380.9 MPa are obtained.
5. A bending angle of 180° is obtained for all the joint specimens, and a crack less than 3 mm is detected.
6. The average values of absorbed energy for the weld are 198.7 and 79.1 J at −40 and −20 °C, respectively. All the specimens exhibit a level of toughness as indicated by deformation at the fracture surface.

References

1. Melchers RE (2004) Effect of small compositional changes on marine immersion corrosion of low alloy steels. Corros Sci 46(7): 1669–1674. doi:10.1016/j.corsci.2003.10.004
2. Yamashita M, Miyuki H, Matsuda Y (1994) The long term growth of the protective rust layer formed on weathering steel by atmospheric corrosion during a quarter of a century. Corros Sci 36(2): 283–289. doi:10.1016/0010-938X(94)90158-9
3. Emilie LG, Muriel C, Remy F (2011) 3D heat transfer model of hybrid laser Nd:Yag-MAG welding of S355 steel and experimental validation. Int J Heat Mass Transf 54(7-8):1313–1322. doi:10.1016/j.ijheatmasstransfer.2010.12.010
4. Mahmoud M, Majid G, Jan F, Alexander F (2013) An investigation on stability of laser hybrid arc welding. Opt Lasers Eng 51(4):481–487. doi:10.1016/j.optlaseng.2012.10.016
5. Cao X, Wanjara P, Huang J, Munro C, Nolting A (2011) Hybrid fiber laser–arc welding of thick section high strength low alloy steel. Mater Des 32(6):3399–3413. doi:10.1016/j.matdes.2011.02.002
6. Liu L, Hao X (2009) Improvement of laser keyhole formation with the assistance of arc plasma in the hybrid welding process of magnesium alloy. Opt Lasers Eng 47(11):1177–1182. doi:10.1016/j.optlaseng.2009.06.003
7. Gleb T, Ekaterina V, Igor T, Alexander L, Olga V (2011) Observation of the mechanisms causing two kinds of undercut during laser hybrid arc welding. Appl Surf Sci 257(17):7501–7506. doi:10.1016/j.apsusc.2011.03.068
8. Song G, An G, Liu L (2012) Effect of gradient thermal distribution on butt joining of magnesium alloy to steel with Cu–Zn alloy interlayer by hybrid laser–tungsten inert gas welding. Mater Des 35: 323–329. doi:10.1016/j.matdes.2011.09.006
9. Stute U, Kling R, Hermsdorf J (2007) Interaction between electrical arc and Nd:YAG laser radiation. Ann CIRP 56(1):197–200. doi:10.1016/j.cirp.2007.05.048
10. Kong F, Ma J, Radovan K (2011) Numerical and experimental study of thermally induced residual stress in the hybrid laser–GMA welding process. J Mater Process Technol 211(6):1102–1111. doi:10.1016/j.jmatprotec.2011.01.012
11. Çam G, Yeni Ç, Erim S, Ventzke V, Koçak M (1998) Investigation into properties of laser welded similar and dissimilar steel joints. Sci Technol Weld Join 3(4):177–189. doi:10.1179/1362171814Y.0000000247
12. Yi SK (2011) Welding materials and microstructure and properties of joint. Chemical Industry Press, Beijing, p 204
13. Çam G, Erim S, Yeni Ç, Koçak M (1999) Determination of mechanical and fracture properties of laser beam welded steel joints. Weld J 78(6):193–201